

Inverting Sediment Bedforms for Exploring the Hazard of Volcanic Density Currents Directly in the Field

Pierfrancesco Dellino (✉ pierfrancesco.dellino@uniba.it)

University of Bari Aldo Moro

Fabio Dioguardi

British Geological Survey

Roberto Sulpizio

University of Bari Aldo Moro

Daniela Mele

University of Bari Aldo Moro

Research Article

Keywords: Pyroclastic density, sediment bedforms, hazard of volcanic density, currents, wavelength and grain size

Posted Date: August 9th, 2021

DOI: <https://doi.org/10.21203/rs.3.rs-777070/v1>

License:  This work is licensed under a Creative Commons Attribution 4.0 International License.

[Read Full License](#)

1 **Inverting sediment bedforms for exploring the hazard of volcanic density currents directly in** 2 **the field**

3 Pierfrancesco Dellino^{1*}, Fabio Dioguardi², Roberto Sulpizio¹ & Daniela Mele¹

4 ¹Dipartimento Di Scienze Della Terra E Geoambientali, Università Di Bari, Bari, Italy. ²British Geological Survey, The
5 Lyell Centre, Edinburgh, UK.
6

7 **Abstract**

8 Pyroclastic density currents are ground hugging gas-particle flows moving at high speed down the
9 volcano slope. They are among the most hazardous events of explosive volcanism, causing
10 devastation and deaths^{1,2}. Because of the hostile nature they cannot be analyzed directly and most of
11 their fluid dynamic behavior is reconstructed by the deposits left in the geological record, which
12 frequently show peculiar structures such as bedforms of the types of ripples and dunes^{3,4}. In this paper,
13 we simplify a set of equations that link flow behavior to particle motion and deposition. This allows,
14 for the first time, the build up of a phase diagram by which the hazard of dilute pyroclastic density
15 currents can be explored easily and quickly by inverting bedforms wavelength and grain size.

16

17 **Main**

18 Geologists and engineers have always been fascinated by sediment bedforms. They are a natural
19 beauty of practical importance and represent a primary resource in the reconstruction of ancient
20 sedimentary environments⁵. They form both in fluvial currents, turbiditic flows, snow avalanches
21 and volcanic pyroclastic density currents (PDCs). When a current flowing over sediment exceeds
22 the critical shear stress for motion, bedforms develop as a result of the interaction between sediment
23 and fluid⁶. The first bedforms to develop are current ripples, which have wavelengths, W_l , smaller
24 than 60 cm⁶. Larger bedforms are called dunes⁷. It is widely recognized that the occurrence of
25 ripples or dunes depends on hydrodynamic conditions and sediment characteristics. These are
26 defined in phase diagrams^{8,9} where bedform characteristics as W_l and sediment median size, D , are

27 related to flow parameters such as the densimetric Froude number Fr'^{10} and the critical Shields
28 number θ_t ¹¹. For symbols see table 1.

29 $Fr' = \frac{V}{\sqrt{g'H}}$ is a balance between inertial and gravitational effects, with $g' = g \left(\frac{\rho_{mix} - \rho_f}{\rho_f} \right)$
30 representing the reduced gravity, g the gravity acceleration, V the current velocity, H the current
31 depth.

$$32 \quad \rho_{mix} = \rho_s C + \rho_f (1 - C) \quad (1)$$

33 is the density of the fluid-particle mixture with ρ_s particle density, ρ_f fluid density and C particle
34 volumetric concentration.

$$35 \quad \theta_t = \frac{\rho_{mix} u_*^2}{Dg(\rho_s - \rho_{mix})} \quad (2)$$

36 is the threshold of initiation of motion of particles resting on the substrate and is a form of shear
37 stress ($\tau = \rho_{mix} u_*^2$, where u_* is the shear velocity) normalized to the sediment static load. It is a
38 function of the Reynolds' number of shear:

$$39 \quad Re_* = \frac{\rho_{mix} u_* D}{\mu} \quad (3)$$

40 where μ is fluid viscosity.

41

42 PDCs form upon explosive eruptions when gases, fragments of magma and lithics, ranging in size
43 from ash to blocks and bombs, are forced throughout the crater to form vertical eruption columns that
44 collapse on the ground or are generated from gravitational failure of domes. They form flows that
45 may spread around the volcano for many kilometers, causing devastation and death. The hazard
46 potential of PDCs depends on impact parameters such as dynamic pressure¹²:

$$47 \quad P_{dyn} = \frac{1}{2} \rho_{mix} V^2 \quad (4)$$

48 that contrasts the resistance of buildings to the flow¹³, and the volumetric concentration of ash
49 particles C , which represents a distinct source of hazard especially far from the volcano where the
50 flow mechanical strength decays, but the current is still rich of ash in suspension. In fact, volcanic

51 ash in the air is very harmful to breath¹⁴, even at temperatures lower than 200°C (that are typical of
52 dilute PDCs), and can cause serious health issues and possibly death to a human being if flow
53 duration, t , which is a proxy for exposure time, is longer than a couple of minutes^{14,15}.
54 Because of the very hostile nature, the behavior of PDCs is difficult to analyze directly, and our
55 understanding is primarily based on the information preserved in the sediments of past eruptions^{2,16,17},
56 laboratory to large-scale experiments^{18,19,20} and numerical modelling^{21,22}. All three methodologies are
57 valid, particularly when they are integrated²³. The former, though, has the advantage of being directly
58 linked to the ground truth when direct observations of the PDCs are not available, provided valid
59 sedimentological models linking deposit characteristics to flow properties and their impact exist¹⁸.
60 Bedforms of the types of dunes and ripples have been widely recognized in the deposits of dilute
61 PDCs since the pioneering observations of Richards²⁴, Moore²⁵ and Fisher and Waters²⁶. Further
62 details on other types of bedforms are nowadays emerging from observation of recent eruptions²⁷.
63 Differently from what has been done for fluvial and turbiditic currents, only very few attempts
64 have been made to construct phase diagrams defining the stability fields of bedforms as a function of
65 PDCs flow regimes. Only very recently Smith et al.¹⁷ have proposed a phase diagram for highly
66 concentrated volcanic granular currents. Dellino et al.²⁸, basing on results of large-scale experiments,
67 have proposed a phase diagram in which volcanic deposits are classified based on their sedimentation
68 rate, S_r and bedload transportation rate, Q_b . This agrees with the approach used in the field of
69 sedimentary currents, for which it is widely recognized that the proportion of bedload to suspended
70 load and the sediment size are the major controlling factors on bedforms formation⁹.

71 S_r is defined by Dellino et al.²⁹, as:

$$72 \quad S_r = \left(\sum_i^n \rho_{s_i} w_{t_i} \left(\frac{\frac{\phi_i / \rho_{s_i} * C}{\sum_{i=1}^n \phi_i / \rho_{s_i} * C}}{\left(\left(10.065 * \frac{P_{ni}}{P_n^*} \right) + 0.1579 \right)} * 0.7 + \frac{\frac{\phi_{i+1} / \rho_{s_{i+1}} * C}{\sum_{i=1}^n \phi_{i+1} / \rho_{s_{i+1}} * C}}{\left(\left(10.065 * \frac{P_{ni}}{P_n^*} \right) + 0.1579 \right)} * 0.3 \right) \right) - 0.01 \quad (5)$$

73 with the subscript i referring to the i_{th} particle-size class and n being the number of size classes of the
74 grain-size distribution of the sediment, where $P_{ni} = w_{ti} / k u_*$ is the Rouse number of the i_{th} size fraction
75 of the solid material suspended in the current, with k the Von Karman constant (0.4) and w_{ti} the

76 terminal velocity of the i_{th} size fraction. $P_n^* = P_{navg}/P_{nsusp}$ is the normalized Rouse number of the
 77 current, i.e. the ratio between the average Rouse number of the solid material in the current and the
 78 Rouse number at maximum suspension capacity. ϕ_i , ρ_{S_i} and P_{ni} are the weight fraction, the density
 79 and the Rouse number of the i_{th} grain-size fraction, respectively. The sedimentation rate was
 80 transformed in the sedimentation rate per unit width, S_{rw} in order to make it comparable with Q_b
 81 dimension²⁸.

82 Q_b is defined by Dellino et al.²⁸ (modified from Wilcock and Crowe³⁰) as:

83 $Q_b = \sum_i^n q_{bi}$ (6)

84 where

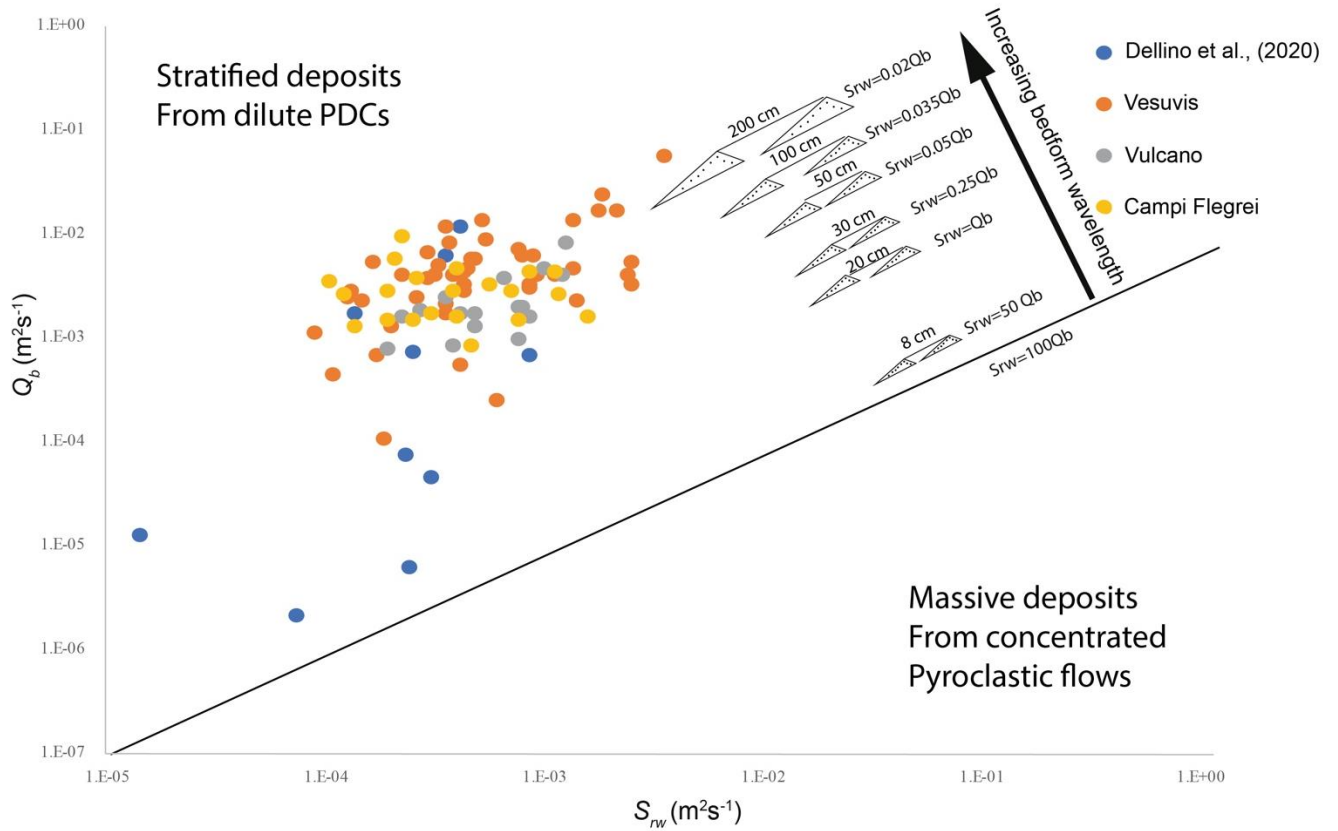
85 $q_{bi} = \frac{(\rho_s/\rho_{mix}-1)gq_{bi}}{W_i^* \phi_i u_*^3}$ and $W_i^* = \begin{cases} 0.002\xi^{7.5} \text{ for } \xi < 1.35 \\ 14 \left(1 - \frac{0.894}{\xi^{0.5}}\right) \text{ for } \xi \geq 1.35 \end{cases}$ (7)

86 q_{bi} is the volumetric bedload transport rate of the i_{th} size fraction per unit width of the flow, and $\xi =$
 87 τ/τ_{ri} is the normalized shear stress, where τ_{ri} is the minimum shear stress needed to move the i_{th}
 88 size fraction at bedload.

89 The lower right portion of the S_{rw} vs Q_b phase diagram of Dellino et al.²⁸ represents the field of
 90 massive deposits due to highly concentrated flows, also known as pyroclastic flows. The upper
 91 portion of the diagram represents the field of stratified deposits with ripple and dune bedforms, which
 92 are related to highly expanded, fast-moving, dilute and turbulent PDCs. W_l of bedforms that
 93 characterize dilute PDCs, shown in the diagram as the distance between two successive dunes or
 94 ripples (in cm), is inversely proportional to the S_{rw}/Q_b ratio, with ripples having a ratio larger than
 95 0.05 and dunes smaller than 0.05.

96 In this paper, we further populate the diagram in the portion of dilute PDCs by adding 88 points
 97 relative to various eruptions of Vesuvius, Campi Flegrei and Vulcano in Italy. With this addition, the
 98 new dataset consists of 98 deposits (Fig. 1) and covers a wide span of the S_{rw} vs Q_b space, allowing

99 an analysis of bedforms in terms of a large range of flow parameters.

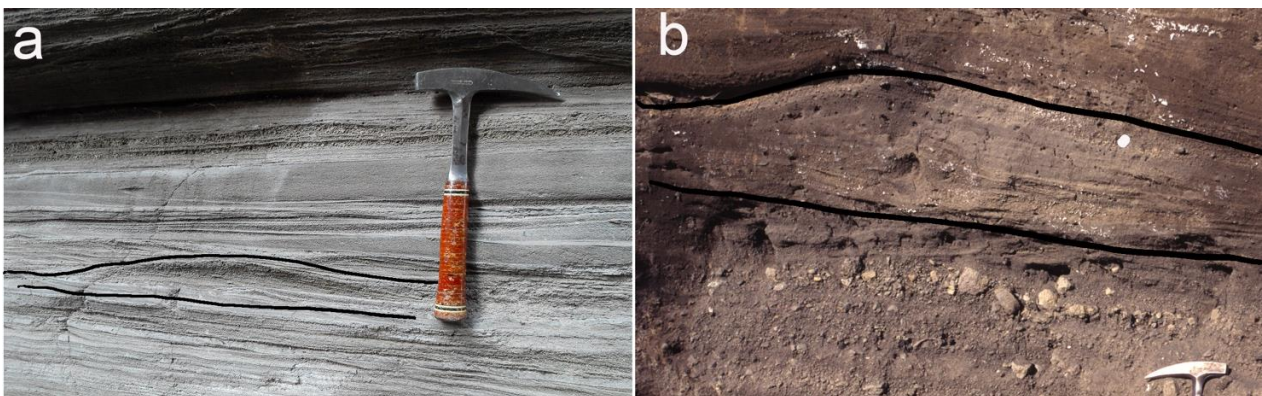


100

101 Fig.1. S_{rw} vs Q_b diagram in which 88 points have been added to those of Dellino et al.²⁸. The W_l of bedforms as a function
 102 of the S_{rw}/Q_b ratio is inserted and also the legend of volcanoes from which deposits were analysed.

103

104 The bedform W_l ranges from ripples (Fig. 2a), starting at 10 cm, to dunes (Fig. 2b), up to 250 cm.



105

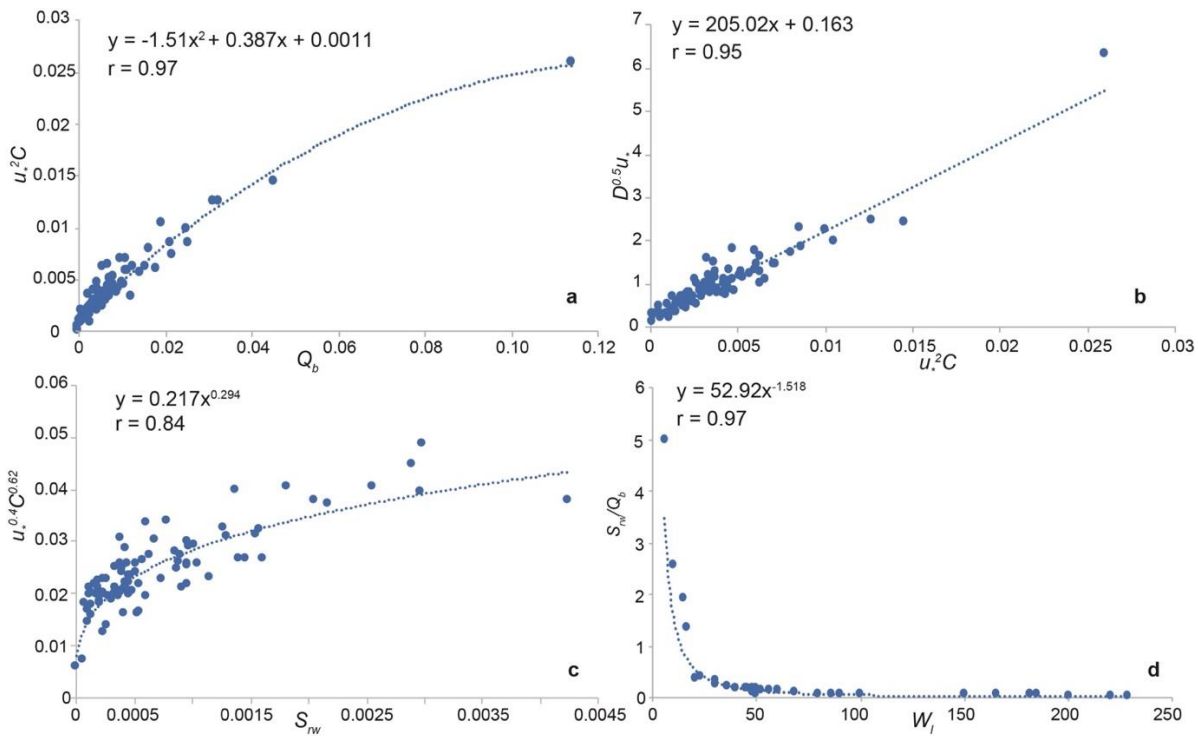
106 Fig. 2. PDC deposits showing bedforms. a=ripples of PDC deposits at Vulcano. The curves enclose a ripple with $W_l =$
 107 40cm. b=a dune bedform of PDC deposits at Vesuvis. The curves enclose a dune with $W_l = 200$ cm.

108

109 We never found antidunes, in fact their interpretation has always been questioned in volcanic
 110 deposits^{11,27}.

111 The software PYFLOW 2.0 by Dioguardi and Mele³¹ has been used to plot data in Fig 1. It was
 112 implemented here so to obtain both the impact parameters of the current together with S_{rw} and Q_b .
 113 The software employs sediment data that result from time-consuming laboratory analyses, which
 114 involve technologies and calculation resources not available to all scientists (see the Method section).
 115 The aim of this paper is to rearrange and simplify the dataset in order to construct a phase diagram
 116 by which to invert W_l and D of PDCs' deposits bedforms and obtain the impact parameters directly
 117 in the field, without the need of the extra terms that require extensive work in the laboratory.

118 By means of regression analysis we obtained three fitting laws (Fig. 3a, b and c) that correlate just
 119 few of the many terms of the formulas of (5), (6) and (7) ($u_*^2 C/Q_b$, $D^{0.5} u_*/u_*^2 C$, $u_*^{0.4} C^{0.62}/S_{rw}$,
 120 respectively), thus reducing the complexity of the original equations, and still guarantee high
 121 correlation coefficients, hence, a good approximation of the full PDCs impact and depositional
 122 models.



123

124 *Fig. 3. Fits resulting from the regression analysis. In the insets both the correlation coefficient, r , and the fitting equation*
 125 *are inset. a=parabolic relationship between $u_*^2 C$ and Q_b . b=linear relationship between $D^{0.5} u_*$ and $u_*^2 C$. c=power-law*
 126 *relationship between $u_*^{0.4} C^{0.62}$ and S_{rw} . d=power-law relationship between S_{rw}/Q_b and W_l .*

127

128 A fourth fitting law between S_{rw}/Q_b vs W_l with a good correlation was obtained by selecting 32
129 deposits characterized by well exposed bedforms ranging between ripples and dunes (Fig. 3d).

130 The fitting laws allow interpreting Q_b and S_{rw} in terms of the deposit formation processes, and also to
131 relate them to the current's flow parameters. In Fig. 3a a relationship between Q_b and Cu_*^2 is shown.

132 Since C is directly proportional to ρ_{mix} and $\rho_{mix}u_*^2$ is the turbulent shear stress of the current³², it
133 means that Q_b is proportional to the shear stress, which confirms the finding of sedimentary currents²⁹.

134 The relationship between Du_* and Cu_*^2 of Fig. 3b implies that shear stress is proportional to bedforms
135 grain size, confirming what reported for sedimentary deposits²⁸. On Fig. 3c a relationship between

136 the product of $C^{0.62}u_*^{0.4}$ and S_{rw} is shown. Since the exponents of C and u_* are both lower than 1,
137 while in the fitting with Q_b of Fig. 3a they are 1 and 2 respectively, it means that with an increase of

138 C and u_* the difference between S_r and Q_b increases, and S_{rw}/Q_b decreases. This justifies that with the
139 decrease of S_{rw}/Q_b , the bedform wavelength increases continuously, as it is shown by Fig. 3d. This

140 outcome deserves an additional comment, because in sedimentary deposits ripples and dunes are not
141 believed to represent a continuum, being them separate by a hydrodynamic discontinuity³³. This

142 happens because ripples, being small, do not interfere with the upper current surface, while dunes,
143 being larger, interfere with it. This discontinuity does not appear in the S_{rw}/Q_b vs W_l diagram of Fig.

144 3d, likely because a true interface between the current and the surrounding atmosphere does not exist
145 in PDCs, which are instead characterized by a very gradual passage between the two¹⁰ (see the method

146 section for our model of dilute PDCs).

147 The four fitting laws make up a system of equations

148
$$u_*^2 C = 1.5099Q_b^2 + 0.3874Q_b + 0.0011$$

149
$$D^{0.5}u_* = 205.02u_*^2 C + 0.163$$

150
$$u_*^{0.4} C^{0.62} = 0.2168S_r^{0.2938} \quad (8)$$

151
$$S_{rw}/Q_b = 52.92W_l^{-1.518}$$

152 that can be solved numerically, once D and W_l are specified, to obtain u_* , C , S_{rw} and Q_b . Important
153 information on the hazard of dilute PDCs can be obtained from the first three parameters. C and u_*
154 serve for the calculation of P_{dyn} (2), since C is used for obtaining ρ_{mix} in (2) by means of (1) and u_*
155 is used for the calculation of V by means of the law of the wall of a turbulent boundary layer³²

$$156 \quad V(y) = u_* \left(\frac{1}{k} \ln \frac{y}{k_s} + 8.5 \right) \quad (9)$$

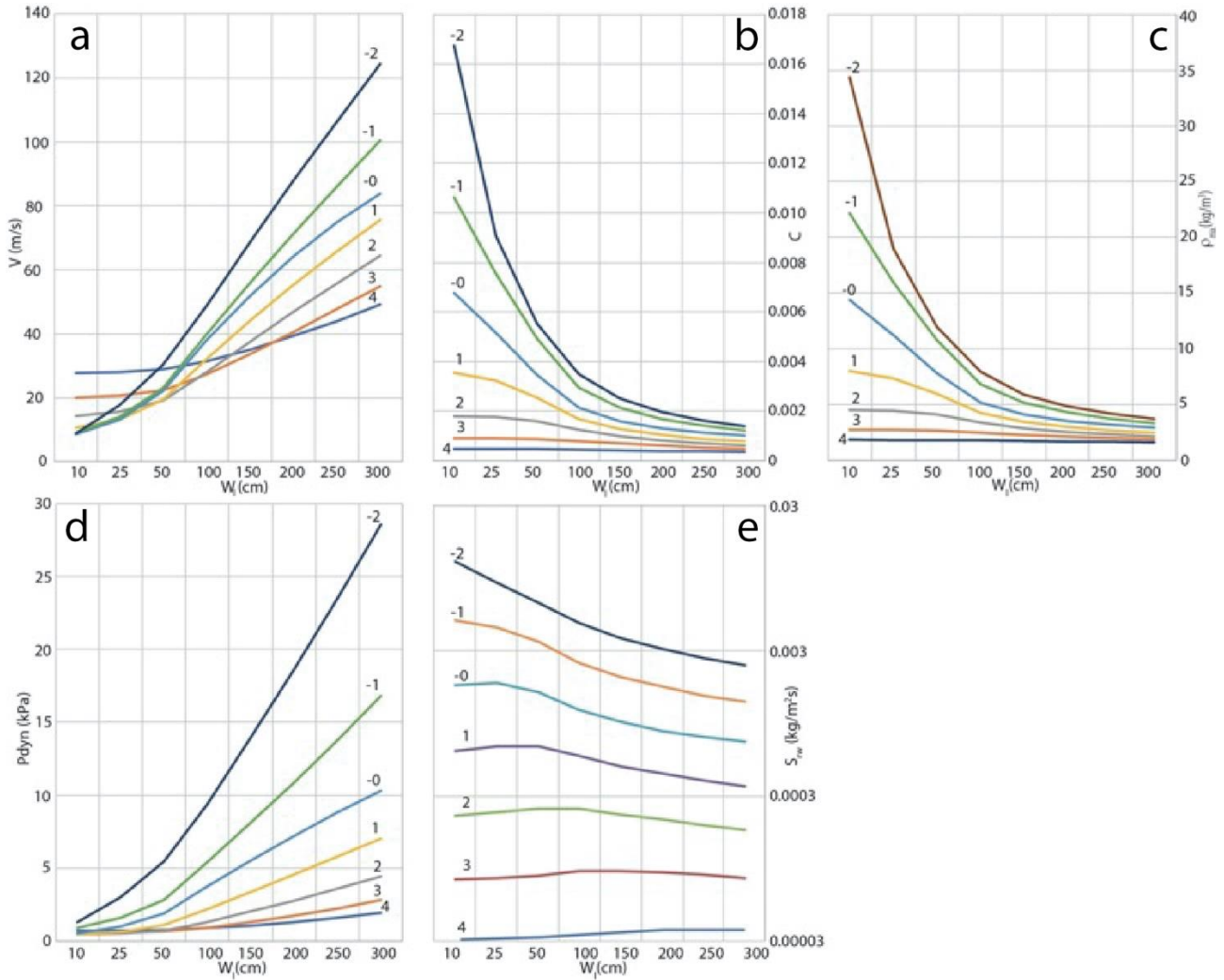
157 which is the physical model of PDCs that we employ (see the method section), where $V(y)$ is the
158 velocity profile of the stratified flow³², and k_s is the substrate roughness.

159 When comparing results obtained by (8) with those resulting from PYFLOW 2, the average absolute
160 error of u_* is 28% and that of C is 30%. This means that a good approximation can be achieved for
161 exploring the range of impact parameters by means of the simplified formulas, without the terms that
162 involve extensive laboratory analysis.

163 The absolute error of S_{rw} is about 45%. While it is larger than that of u_* and C , we discuss also the
164 role of S_{rw} because it allows the calculation of flow duration, t^{15} , which is an important factor of
165 hazard. The total time of aggradation is a proxy of flow duration, t , which is equal to deposit thickness,
166 H_{dep} , divided by A_r , the aggradation rate. Sedimentation occurs by continuous aggradation during the
167 passage of the current, and A_r is equal to S_{rw} divided by one meter, which is the reference width of
168 the sedimentation rate per unit width, (see Dellino et al.²⁸). Therefore, flow duration, which
169 approximates the time in which harmful concentrations of ash are suspended in the current to which
170 a human being can be exposed, can be calculated by means of S_{rw} . With our model a reasonable
171 approximation can be achieved also on such a relevant parameter of PDCs.

172 In Fig. 4, which was constructed by means of (8), the main flow variables and impact parameters are
173 shown as a function of D and W_l . The W_l range was set between 10 and 300 cm. Bedforms with larger
174 W_l can be found in the geologic record of volcanic deposits, but this scenario is out of the range of
175 applicability of our model. We are, in fact, considering bedforms that develop on an almost flat
176 surface. Much larger bedforms, instead, typically develop as an interplay between the current's flow

177 dynamics and large ground morphology elements²⁷ (e.g. ridges, big obstacles). The range of D of Fig.
 178 4 was set between 4 and -2 phi (0.0064 mm and 4 mm respectively). We do not include coarser values
 179 because, in volcanic sediments, larger sizes (coarse lapilli and bombs) do not form dunes, but
 180 lenticular beds representing highly concentrated traction-carpets at the base of PDCs^{34,35}, to which
 181 our model does not apply.



182

183 *Fig. 4. Trends of flow variables and impact parameters of dilute PDCs as a function of bedform wavelengths. The various*
 184 *curves represent the behavior of different grain size D . Grain size is expressed in phi units ($\phi = -\log_2 D$, with D in mm).*
 185 *a=trend of velocity, V , height-averaged in the first 1000 cm of the current in relation to W_l . b=trend of concentration C ,*
 186 *in relation to W_l . c=trend of gas-particle mixture density ρ_{mix} in relation to W_l . d=trend of dynamic pressure, P_{dyn} in*
 187 *relation to W_l . e=trend of sedimentation rate S_{rw} , in relation to W_l .*
 188

189 In Fig. 4a the value of velocity V , as averaged in the first 1000 cm of the current, which was obtained
 190 by integrating (9) over flow height, with $k_s = 10$ cm, is plotted against W_l . We chose this depth-
 191 averaging height because, in dilute PDCs, the portion responsible for the dynamic impact is the

192 lowermost one (the shear flow) and 1000 cm represent a reasonable estimate of an average building
193 height³⁶. V increases at increasing W_l but with different trends and rates depending on the particle
194 grain size D . In the diagram it ranges from about 10 m/s to about 130 m/s. The trends are significantly
195 different for the finer grain sizes (1 to 4 phi) at the smallest W_l (up to 50 cm), which can be interpreted
196 as the smaller it is W_l , the smaller are Q_b and shear stress, therefore the higher the velocity required
197 to develop bedforms with the finest D . This is because for fine ash, due to the very low Re_* , the
198 initiation of motion at the bedload occurs at a very high θ_t ^{29,37}. With larger W_l , corresponding to
199 larger Q_b and larger shear stress, higher velocities are needed with coarser particles, because θ_t
200 decreases down to the constant value characteristic of high Re_* ³⁷, which in turn implies that a larger
201 shear stress is needed to move larger grain sizes. The volumetric concentration, C , ranges from less
202 than 0.001 to about 0.017 (Fig. 4b). It decreases as W_l increases, and it does so for all grain sizes,
203 although at a rate that decreases at decreasing D , because a higher concentration favors a higher S_{rw}
204 (see (7)) and a larger S_{rw}/Q_b ratio, hence a smaller W_l . The evident change in trend with decreasing
205 grain size can be explained by the fact that the finer the particles, the lower the concentration required
206 to develop bedforms with small wavelengths; the increase of shear stress and Q_b results in similar
207 concentrations for all grainsizes. The density of the current (Fig. 4c) follows the trend of
208 concentration, as it is calculated by means of (1) and fixing $\rho_s = 2000 \text{ kg/m}^3$ and $\rho_f = 0.9 \text{ kg/m}^3$ (which
209 is reasonable if the fluid, made up of volcanic gas plus entrained cold atmosphere, is at about 200 °C
210 ¹⁸) and varies from less than 2 kg/m^3 to about 35 kg/m^3 . By using the values of density and velocity
211 in (4) the trend of P_{dyn} is shown in Fig. 4d. It varies from less than 1 kPa with smaller W_l and finer D ,
212 which is a value that does not cause severe damages to buildings^{1,13}, to almost 30 kPa with larger W_l
213 and coarser D , which can destroy even the more resistant, modern buildings of reinforced concrete^{1,13}.
214 The sedimentation rate (Fig. 4e) increases as grain size coarsens, meaning that with finer sizes flow
215 duration is longer, as it is expected since finer sizes result in a smaller settling velocity. As far as the
216 wavelength is concerned, for the finest sizes, S_{rw} increases at increasing W_l , meaning a decrease of

217 flow duration with longer bedforms. With the coarsest sizes, instead, the sedimentation rate decreases
218 as W_l increases, meaning a longer flow duration with longer bedforms.

219 The ranges of W_l and D used in (8) for obtaining the trends of Fig. 4 replicate the ranges in our dataset,
220 and result in parameters that span from currents that do not impact severely on structures, to values
221 of devastating effects. Such a range well represents the situation of large-scale PDCs whose strength
222 decreases along runout¹⁵, and change from totally destructive flows around the volcano to residual
223 currents that in the distal outreach do not possess a high strength but can still be rich of ash. Such fine
224 glassy material can be highly dangerous to breath even at concentrations lower than 0.001³⁸ if flow
225 duration t , which can be calculated by means of S_{rw} , lasts more than a couple of minutes. Thus, with
226 our model it is possible to invert bedforms of past eruptions, and follow the different aspects of PDCs
227 hazard as they evolve along flow runout.

228 In order to help scientists not availing of numerical resources to take advantage of our results, we
229 solved (8) at discrete intervals of D and W_l and constructed a phase diagram where the stability fields
230 of P_{dyn} , C and S_{rw} are represented inside a grid (Fig. 5). The values are averaged among the four
231 neighboring grid points and the uncertainty is expressed in terms of one standard deviation. P_{dyn} is
232 calculated by considering the average value obtained by integration over the first 1000 cm of the
233 current, and setting $k_s = 10$ cm and $\rho_s = 2000$ kg/m³.

		Grain size (ϕ)								
		4	3	2	1	0	-1	-2		
wavelength (m)	3	P_{dyn} (kPa)	2.14±0.51	3.27±0.96	5.21±1.50	7.98±1.98	12.4±3.57	20.6±6.66	P_{dyn} (kPa)	3
		C	4.3E-4±9.0E-5	5.9E-4±9.7E-5	7.5E-4±1.1E-4	9.5E-4±1.5E-4	1.2E-3±1.7E-4	1.4E-3±1.7E-4	C	
		S_{rw} (m ² s ⁻¹)	6.0E-5±2.8E-5	1.3E-4±5.7E-5	2.7E-4±1.0E-4	5.5E-4±2.1E-4	1.1E-3±3.9E-4	2.0E-3±6.6E-4	S_{rw} (m ² s ⁻¹)	2.5
	2.5	P_{dyn} (kPa)	1.72±0.39	2.60±0.79	4.18±1.28	6.60±1.84	10.2±2.82	16.7±5.55	P_{dyn} (kPa)	2.5
		C	4.8E-4±1.1E-4	6.7E-4±1.2E-4	8.6E-4±1.4E-4	1.1E-3±1.8E-4	1.4E-3±2.4E-4	1.7E-3±2.3E-4	C	
		S_{rw} (m ² s ⁻¹)	6.2E-5±3.0E-5	1.4E-4±6.3E-5	2.9E-4±1.2E-4	6.0E-4±2.3E-4	1.2E-3±4.5E-4	2.2E-3±7.7E-4	S_{rw} (m ² s ⁻¹)	2
	2	P_{dyn} (kPa)	1.35±0.28	1.96±0.63	3.19±1.06	5.17±1.63	7.93±2.24	12.9±4.51	P_{dyn} (kPa)	2
		C	5.3E-4±1.4E-4	7.8E-4±1.6E-4	1.0E-3±2.9E-4	1.3E-3±2.3E-4	1.7E-3±3.4E-4	2.1E-3±3.4E-4	C	
		S_{rw} (m ² s ⁻¹)	6.2E-5±3.2E-5	1.5E-4±7.2E-5	3.3E-4±1.4E-4	6.8E-4±2.7E-4	1.4E-3±5.4E-4	2.6E-3±9.2E-4	S_{rw} (m ² s ⁻¹)	1.5
	1.5	P_{dyn} (kPa)	1.04±0.18	1.39±0.46	2.23±0.84	3.70±1.37	5.68±1.80	9.20±3.55	P_{dyn} (kPa)	1.5
		C	5.9E-4±1.8E-4	9.3E-4±2.4E-4	1.3E-3±2.9E-4	1.7E-3±3.6E-4	2.2E-3±5.6E-4	2.8E-3±5.9E-4	C	
		S_{rw} (m ² s ⁻¹)	6.2E-5±3.3E-5	1.6E-4±8.3E-5	3.8E-4±1.7E-4	7.9E-4±3.2E-4	1.6E-3±7.0E-4	3.2E-3±1.2E-3	S_{rw} (m ² s ⁻¹)	1
	1	P_{dyn} (kPa)	0.81±0.12	0.91±0.30	1.34±0.62	2.23±1.09	3.47±1.50	5.77±2.69	P_{dyn} (kPa)	1
		C	6.4E-4±2.2E-4	1.1E-3±3.7E-4	1.8E-3±5.5E-4	2.4E-3±7.5E-4	3.4E-3±1.2E-3	4.2E-3±1.2E-3	C	
		S_{rw} (m ² s ⁻¹)	6.0E-5±3.2E-5	1.7E-4±9.0E-5	4.3E-4±2.1E-4	9.8E-4±4.5E-4	2.1E-3±1.0E-3	4.2E-3±1.7E-3	S_{rw} (m ² s ⁻¹)	0.5
	0.5	P_{dyn} (kPa)	0.68±0.08	0.63±0.09	0.76±0.25	1.16±0.53	1.82±0.77	3.22±1.63	P_{dyn} (kPa)	0.5
		C	6.7E-4±2.5E-4	1.3E-3±4.6E-4	2.3E-3±7.5E-4	3.6E-3±1.1E-3	5.3E-3±1.7E-3	6.8E-3±1.9E-3	C	
		S_{rw} (m ² s ⁻¹)	5.7E-5±3.0E-5	1.6E-4±8.9E-5	4.5E-4±2.4E-4	1.2E-3±5.8E-4	2.8E-4±1.3E-3	5.7E-3±2.4E-3	S_{rw} (m ² s ⁻¹)	0.25
0.25	P_{dyn} (kPa)	0.64±0.09	0.53±0.04	0.53±0.08	0.65±0.24	0.99±0.43	1.70±0.92	P_{dyn} (kPa)	0.25	
	C	6.9E-4±2.5E-4	1.3E-4±5.0E-4	2.6E-4±9.4E-4	4.7E-3±1.6E-3	7.5E-3±2.3E-3	1.1E-2±4.0E-3	C		
	S_{rw} (m ² s ⁻¹)	5.6E-5±2.9E-5	6.0E-5±2.8E-5	4.3E-4±2.4E-4	1.2E-3±6.5E-4	3.1E-3±1.6E-3	7.5E-3±3.7E-3	S_{rw} (m ² s ⁻¹)	0.1	
0.1		4	3	2	1	0	-1	-2		

234

235 *Fig. 5. Phase diagram in which the stability fields of the impact parameters P_{dyn} , C and S_{rw} , are expressed as a function*
 236 *of W_l and D of bedforms. The values inside the grid represent the average between the four neighboring grid points and*
 237 *the uncertainty is expressed as the standard deviation. $K_s = 10$ cm, $\rho_s = 2000$ kg/m³.*
 238

239 In the supplementary Information, additional diagrams with $k_s = 10$ cm and $\rho_s = 1000$ kg/m³ ; $k_s = 30$
 240 cm and $\rho_s = 2000$ kg/m³ ; and $k_s = 10$ cm and $\rho_s = 1000$ kg/m³ are included (Supp. Fig. 1,2 and 3
 241 respectively), and a table is also provided (Supp. Tab.1) where the values of u_* , C and S_r are set at
 242 half phi intervals of D in relation to W_l . By means of these data, and specifying in (4) and (9) the
 243 value of k_s , ρ_s , and H at which to integrate V , more precise data of the impact parameters can be
 244 obtained.

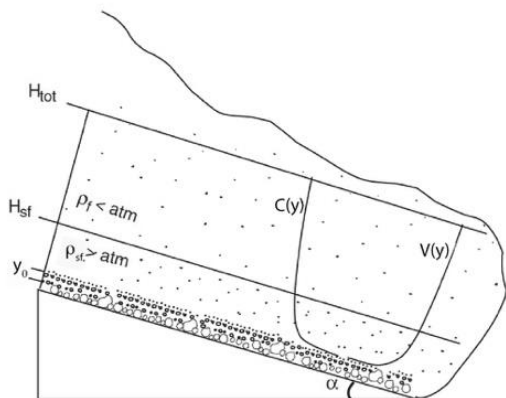
245 With our diagrams and tables at hand it is thus possible for every scientist working on hazardous
 246 volcanoes to make an exploratory hazard assessment by means simply of the wavelength and grain
 247 size of bedforms. It is true that bedforms are not always well exposed in their complete longitudinal
 248 profile, because of truncations due to erosion. Sometimes they are also difficult to measure precisely,

249 because a direct access to the deposit is hard. Anyway, our experience tells that dilute PDCs most
250 always leave well-preserved bedforms as a trace of their passage. Scientists working on active
251 volcanoes are encouraged to look for good outcrops where bedforms can be measured. By means of
252 our phase diagrams, now they have a tool for exploring the behavior of hazardous pyroclastic density
253 currents directly in the field.

254

255 Method

256 The reconstruction of the impact parameters of PDCs is based on a flow mechanical model that starts
257 with the assumption that the turbulent current is velocity and density stratified^{12,40}. In the stratified
258 multiphase gas-particle current, the basal part is a shear flow that moves attached to the ground and
259 has a density higher than atmosphere (Fig. 6). The upper part is buoyant, because particle
260 concentration decreases with height down to a value that, combined with the effect of gas temperature,
261 makes the mixture density lower than the surrounding atmosphere.



262

263 *Fig. 6. Sketch of the model of a pyroclastic density current used in this paper*

264

265 In a PDC, particles are mainly transported by turbulent suspension and sedimentation is controlled
266 by a balance between flow shear velocity u^* , which is controlled by fluid turbulence and favors
267 suspension, and particle settling velocity, $w_t = (4gD(\rho_s - \rho_{mix})/3C_d\rho_{mix})^{0.5}$, which favors sedimentation,
268 where C_d is drag coefficient. During sedimentation, it is assumed that particles of different
269 composition, i.e. crystals and glass, settle at the same aerodynamic conditions, e.g., with the same

270 terminal velocity¹⁵. Therefore, by equating the settling velocity of the glass and crystal components
 271 in the deposit, and assuming that sedimentation starts when $P_n = 2.5$, hence when $w_t = u_*$, flow shear
 272 velocity and density ρ_{sf} of the shear flow can be calculated after D , ρ_s and C_d are measured in the
 273 laboratory³⁶. These are the main input data in the PYFLOW_2.0 code³¹, which allows reconstructing
 274 the current parameters.

275 The code is based on a model that assumes PDCs behave as turbulent boundary layer shear flows
 276 moving over a rough surface³⁷, which velocity profile is given by (9). The model has been validated
 277 by experiments¹⁸ and already applied to other eruptions^{40,41}. Here it is summarized as adapted from
 278 Dellino et al.¹⁵.

279 The maximum volumetric concentration of particles that can be transported in turbulent suspension,
 280 i.e. the maximum current capacity, is a function of the Rouse number of the particulate mixture taken
 281 in suspension. The profile of volumetric concentration over current height is regulated by the Rouse
 282 model⁴².

$$283 \quad C(y) = C_0 \left(\frac{y_0}{H-y_0} \frac{H-y}{y} \right)^{P_n} \quad (10)$$

284 where C_0 is the particle volumetric concentration at a reference height y_0 and H is the total current
 285 thickness. Assuming steady sedimentation, H is obtained by the ratio H_{dep}/C_{sf} where H_{dep} is deposit
 286 thickness and C_{sf} is the depth-averaged concentration in the basal shear flow, which can be calculated
 287 by $\rho_{sf} = \rho_s C_{sf} + \rho_f (1 - C_{sf})$, when ρ_{sf} and ρ_f are known.

288 The shear-flow height and density are obtained by solving the system of (11) and (12), which is valid
 289 for a turbulent current

$$290 \quad \tau = (\rho_{sf} - \rho_f) g \sin \alpha H_{sf} \quad (11)$$

$$291 \quad \tau = \rho_{sf} u_*^2 \quad (12)$$

292 where τ is the shear-driving stress of the flow moving down an inclined slope of angle α .

293 The density profile, which is a function of concentration, particle density and gas density, is:

$$294 \quad \rho_{mix}(y) = \rho_f + C_0 \left(\frac{y_0}{H-y_0} \frac{H-y}{y} \right)^{P_n} (\rho_s - \rho_f) \quad (13)$$

295 The gas density and Rouse number are obtained by solving numerically the following system:

$$296 \quad \rho_a(y) = \rho_f + C_0 \left(\frac{y_0}{H-y_0} \frac{H-H_{sf}}{H_{sf}} \right)^{P_n} (\rho_s - \rho_f) \quad (14)$$

$$297 \quad \rho_{sf} = \frac{1}{H_{sf}-y_0} \int_{y_0}^{H_{sf}} \left(\rho_f + C_0 \left(\frac{y_0}{H-y_0} \frac{H-y}{y} \right)^{P_n} (\rho_s - \rho_f) \right) dy \quad (15)$$

298 Equation (14) states that atmospheric density, ρ_a , is reached at the top of the shear flow, H_{sf} , and
299 equation (15) states that the average density of the shear flow, ρ_{sf} refers to the part of the flow that
300 goes from the reference level, y_0 , to the shear flow top height, H_{sf} .

301 By combining the velocity and density profiles, the dynamic pressure profile is finally obtained. The
302 profiles of the flow parameters are expressed in terms of a probability density function that depends
303 on the variance of particle characteristics.

304

305 **References**

- 306 1. Spence, R. J.S., Baxter, P. J. & Zuccaro G. Building vulnerability and human casualty
307 estimation for a pyroclastic flow: A model and its application to Vesuvius. *J. Volcanol.*
308 *Geotherm. Res.* **133**, 321–343 (2004).
- 309 2. Sulpizio, R., Dellino, P., Doronzo, D. M. & Sarocchi, D. Pyroclastic density currents: state of
310 the art and perspectives. *J. Volcanol. Geotherm. Res.* **283**, 36–65 (2014).
- 311 3. Chough, S.K. & Sohn, Y.K. Depositional mechanics and sequences of base surges, Songaksan
312 tuff ring, Cheju Island, Korea. *Sedimentology* **37**(6), 1115-1135 (1990).
- 313 4. Douillet, G.A. The supercritical question for pyroclastic dune bedforms: An overview.
314 *Sedimentology* (2021). doi.org/10.1111/sed.12859
- 315 5. Middleton, G.V. & Southard, J.B. *Mechanics of Sediment Movement*, 2nd edn. Society of
316 Economic Paleontologists and Mineralogists, Tulsa, OK, 401 pp (1984).
- 317 6. Bartholdy, J., Ernsten, V.B., Flemming, B.W., Winter, C., Bartholomä, A. & Kroon, A. On
318 the formation of current ripples. *Sci. Rep.* **5**, 11390 (2015). doi:10.1038/srep11390
- 319 7. Ashley, G.M. Classification of large-scale subaqueous bedforms: a new look at an old
320 problem: bedforms and bedding structures: *J. Sed. Pet.* **60**, 160–172 (1990).
- 321 8. Perillo, M.M., Best, J.L. & Garcia, M.H. A new phase diagram for combined-flow bedforms.
322 *J. Sed. Res.* **84**, 301-313 (2014).
- 323 9. Fedele, J.J., Hoyal, D.C., Barnaal, Z., Tulenko, J. & Awalt, S. Bedforms created by gravity
324 flows. In: In: Budd, D., Hajek, E., Purkis, S. (Eds.), *Autogenic Dynamics and Self-*
325 *Organization in Sedimentary Systems* 106. SEPM Spec. Pub. 95–121 (2016).
- 326 10. Middleton, G.V. (1993). Sediment deposition from turbidity currents. *Annu. Rev. Earth*
327 *Planet. Sci.* **21**, 89-114 (1993).
- 328 11. Allen J.R.L. *Sedimentary Structures, their Character and Physical Basis. Developments in*
329 *Sedimentology*, vol. **30A**, Elsevier (1982).
- 330 12. Valentine, G.A. Damage to structures by pyroclastic flows and surges, inferred from nuclear
331 weapons effects. *J. Volcanol. Geoth. Res.* **87**, 117–140 (1998).

- 332 13. Zuccaro, G., Cacace, F., Spence, R.J.S. & Baxter, P.J. Impact of explosive eruption scenarios
333 at Vesuvius. *J. Volcanol. Geotherm. Res.* **178**, 416–453 (2008).
- 334 14. Baxter, P.J., Jenkins, S., Rosadi, S., Komorowski, J.-C., Dunn, K., Purser, D., Voight, B. &
335 Shelley, I. Human survival in volcanic eruptions: thermal injuries in pyroclastic surges, their
336 causes, prognosis and emergency management. *Burns* **43**, 1051-1069 (2017).
- 337 15. Dellino P., Dioguardi F., Isaia R., Sulpizio R., Mele D. The impact of pyroclastic density
338 currents duration on humans: the case of the AD 79 eruption of Vesuvius. *Sci. Rep.* **11**(1),
339 4959 (2021).
- 340 16. Branney, M.J. & Kokelaar, P. Pyroclastic density currents and the sedimentation of
341 ignimbrites. *Geol Soc London Memoir* **27**, 1–143 (2002).
- 342 17. Smith, G., Rowley, P., Williams, R., Giordano, G., Trolese, M., Silleni, A., Parsons, D.R. &
343 Capon, S. A bedform phase diagram for dense granular currents. *Nat. Commun.* **11**(1), 1-11
344 (2020).
- 345 18. Dellino, P., Büttner, R., Dioguardi, F., Doronzo, D.M., La Volpe, L., Mele, D., Sonder, I.,
346 Sulpizio, R. & Zimanowki, B. Experimental evidence links volcanic particle characteristics
347 to pyroclastic flow hazard. *Earth Planet. Sci. Lett.* **295**, 314-320 (2010). doi:
348 10.1016/j.epsl.2010.04.022
- 349 19. Andrews, B.J. Recognizing unsteadiness in the transport systems of dilute pyroclastic
350 density currents. *Bull. Volcanol.* **81**(2), 5 (2019).
- 351 20. Brosch, E. & Lube, G. Spatiotemporal sediment transport and deposition processes in
352 experimental dilute pyroclastic density currents. *J. Volcanol. Geotherm. Res.* **401**, 106946
353 (2020).
- 354 21. Doronzo, D.M., Dellino, P., Sulpizio, R., Lucchi, F. Merging field mapping and numerical
355 simulation to interpret the lithofacies variations from unsteady pyroclastic density currents
356 on uneven terrain: The case of La Fossa di Vulcano (Aeolian Islands, Italy). *J. Volcanol.*
357 *Geotherm. Res.* **330**, 36-42 (2017).
- 358 22. Tadini, A., Bevilacqua, A., Neri, A., Cioni, R., Biagioli, G., de' Michieli Vitturi, M., Esposti
359 Ongaro, T. Reproducing pyroclastic density current deposits of the 79 CE eruption of the
360 Somma-Vesuvius volcano using the box-model approach. *Solid Earth* **12**, 119-139 (2021).
- 361 23. Doronzo, D.M., de Tullio, M.D., Pascazio, G., Dellino, P., Liu, G. On the interaction
362 between shear dusty currents and buildings in vertical collapse: Theoretical aspects,
363 experimental observation, and 3D numerical simulation. *J. Volcanol. Geotherm. Res.* **302**,
364 190-198 (2015).
- 365 24. Richards, A.F. Geology of the islas revillagigedo, mexico. *Bull. Volcanol.* **22**(1), 73 (1959).
- 366 25. Moore, J.G. Base surge in recent volcanic eruptions. *Bull. Volcanol.* **30**(1), 337 (1967).
- 367 26. Fisher, R.V. & Waters, A.C. Bed forms in base-surge deposits: Lunar implications. *Science*
368 **165**(3900), 1349-1352 (1970).
- 369 27. Douillet, G.A., Bernard, B., Bouysson, M., Chaffaut, Q., Dingwell, D.B., Gegg, L., Hoelscher,
370 I., Kueppers, U., Mato, C., Ritz, V.A. & Schlunegger, F. Pyroclastic dune bedforms:
371 macroscale structures and lateral variations. Examples from the 2006 pyroclastic currents at
372 Tungurahua (Ecuador). *Sedimentology* **66**(5), 1531-1559 (2019).
- 373 28. Dellino, F., Dioguardi, F., Doronzo, D.M. & Mele, D. A discriminatory diagram of massive
374 vs stratified deposits based on the sedimentation and bedload transportation rates.
375 Experimental investigation and application to pyroclastic density currents. *Sedimentology* **67**
376 (4), 2013-2039 (2020). doi:10.1111/sed.12693.
- 377 29. Dellino, P., Dioguardi, F., Doronzo, D.M. & Mele, D. The rate of sedimentation from
378 turbulent suspension: an experimental model with application to pyroclastic density currents
379 and discussion on the grain-size dependence of flow mobility. *Sedimentology* **66**(1), 129-145
380 (2019). doi:10.1117sed.12485.
- 381 30. Wilcock, P.R. & Crowe, J.C. Surface-based transport model for mixed-size sediment. *J.*
382 *Hydraul. Eng.* **129**, 120–128 (2003).

- 383 31. Dioguardi, F. & Mele, D. PYFLOW_2.0: A computer program for calculating flow properties
384 and impact parameters of past dilute pyroclastic density currents based on field data. *Bull.*
385 *Volcanol.* **80**(3), 28 (2018). doi:10.1007/s00445-017-1191-z.
- 386 32. Furbish, D.J. *Fluid Physics in Geology*. *Oxford University Press*, New York, Oxford. 476 pp
387 (1997).
- 388 33. de Cala, I., Ohata, K., Dorrell, R., Naruse, H., Patacci, M., Amy, L.A., Simmons, S.,
389 McLelland, S.J. & McCaffrey, W.D. Relating the Flow Processes and Bedforms of Steady-
390 State and Waning Density Currents. *Front. Earth Sci.* **8**, 535743 (2020). doi:
391 10.3389/feart.2020.535743.
- 392 34. Sohn, Y.K. On traction-carpet sedimentation. *J. Sed. Res.* **67**, 502–509 (1997).
- 393 35. Dellino, P., Isaia, R., La Volpe, L. & Orsi, G.. Interaction between particles transported by
394 fallout and surge in the deposits of the Agnano-Monte Spina eruption (Campi Flegrei,
395 Southern Italy). *J. Volcanol. Geotherm. Res.* **133**, 193-210 (2004).
- 396 36. Dellino, P., Mele, D., Sulpizio, R., La Volpe, L. & Braia, G. A method for the calculation of
397 the impact parameters of dilute pyroclastic density currents based on deposit particle
398 characteristics. *J. Geophys. Res.* **113**, B07206 (2008). doi:10.1029/2007JB005365.
- 399 37. Miller, M.C., McCave, I.N. & Komar, P.D. Threshold of sediment motion under
400 unidirectional currents. *Sedimentology* **24**, 507–527 (1977).
- 401 38. Jenkins, S., Komorowski, J.C., Baxter, P.J., Spence, R., Picquout, A., Lavigne, F. & Surono.
402 The Merapi 2010 eruption: An interdisciplinary impact assessment methodology for
403 studying pyroclastic density current dynamics. *J. Volcanol. Geotherm. Res.* **261**, 316–329
404 (2013).
- 405 39. Brown, R.J. & Branney, M.J. Internal flow variations and diachronous sedimentation within
406 extensive, sustained, density stratified pyroclastic density currents down gentle slopes, as
407 revealed by the internal architectures of ignimbrites in Tewnerife. *Bull. Volcanol.* **75**, 1–24
408 (2013).
- 409 40. Dellino, P., Mele, D., Bonasia, R., Braia, G., La Volpe, L. & Sulpizio, R. The analysis of the
410 influence of pumice shape on its terminal velocity. *Geophys. Res. Lett.* **32**, L21306 (2005).
- 411 41. Mele, D., Dioguardi, F., Dellino, P., Isaia, R., Sulpizio, R. & Braia, G. Hazard of pyroclastic
412 density currents at the Campi Flegrei Caldera (Southern Italy) as deduced from the combined
413 use of facies architecture, physical modeling and statistics of the impact parameters. *J.*
414 *Volcanol. Geotherm. Res.* **299**, 35–53 (2015).
- 415 42. Rouse, H. An analysis of sediment transportation in the light of fluid turbulence. *Soil*
416 *Conservation Services Report No. SCS-TP-25*, USDA, Washington, D.C (1939).
- 417
- 418
- 419
- 420
- 421
- 422
- 423
- 424
- 425

Symbol	description	dimension
A_r	Aggradation rate per unit width	ms^{-1}
C	Particle volumetric concentration	-
C_0	Reference known concentration (0.75)	-
C_{sf}	Depth-averaged concentration in the basal shear flow	-
C_d	Particle drag coefficient	-
D	Sediment median size	mm
Fr'	Froude number	-
g	Gravity acceleration (9.81)	ms^{-2}
H	Current depth	cm
H_{dep}	Deposit thickness	cm
k	Von Karman constant (0.4)	-
k_s	Substrate roughness	cm
P_{dyn}	Dynamic pressure	Pa
P_n	Particle Rouse number	-
P_n^*	Normalized Rouse number	-
P_{navg}	Average Rouse number of solid material	-
P_{ni}	Rouse number of the i th particle-size class	-
P_{nsusp}	Rouse number at maximum suspension capacity	-
Q_b	Bedload transportation rate	m^2s^{-1}
q_{bi}	Volumetric bedload transport rate of the i th particle-size class	m^2s^{-1}
Re^*	Reynolds' number	-
S_r	Sedimentation rate	$\text{kgm}^{-2}\text{s}^{-1}$
S_{rw}	Sedimentation rate per unit width	m^2s^{-1}
t	Flow duration	s
u^*	Shear velocity	ms^{-1}
V	Current velocity	ms^{-1}
W_i^*	Dimensionless transport rate of the i th particle-size class	-
W_l	wavelength	cm
w_l	Particle terminal velocity	ms^{-1}
w_{li}	Terminal velocity of the i th particle-size class	ms^{-1}
y	Flow vertical coordinate	cm
y_0	Specific height of C_0	-
α	Slope angle	°
ϕ	Unit of grain-size distribution ($\phi = -\log_{2d}$; d is in mm)	-
ϕ_i	Weight fraction of the i_{th} size class	Weight%
θ_t	Shield's number	-
μ	Fluid viscosity	Pas
ρ_f	Fluid density	kgm^{-3}
ρ_{mix}	Density of the fluid-particle mixture	kgm^{-3}
ρ_s	Particle density	kgm^{-3}
ρ_{sf}	Density of shear flow	kgm^{-3}
ρ_{si}	Density of the i th particle-size class	kgm^{-3}
τ	Shear stress at the base of the current	Pa
τ_{ri}	Minimum shear of the i_{th} size fraction	Pa
ξ	Normalized shear stress	-

Supplementary Files

This is a list of supplementary files associated with this preprint. Click to download.

- [Suppfig1.pdf](#)
- [Suppfig2.pdf](#)
- [Suppfig3.pdf](#)
- [SupplTab.pdf](#)